

# Influence of Heat Treatments on Microstructure and Magnetic Domains in Duplex Stainless Steel S31803



JEAN DILLE, CLARA JOHANNA PACHECO, CESAR GIRON CAMERINI, LOIC CHARLES MALET, BERNARD NYSTEN, GABRIELA RIBEIRO PEREIRA, LUIZ HENRIQUE DE ALMEIDA, and JOÃO MARCOS ALCOFORADO REBELLO

The influence of heat treatments on microstructure and magnetic domains in duplex stainless steel S31803 is studied using an innovative structural characterization protocol. Electron backscatter diffraction (EBSD) maps as well as magnetic force microscopy (MFM) images acquired on the same region of the sample, before and after heat treatment, are compared. The influence of heat treatments on the phase volumetric fractions is studied, and several structural modifications after heat treatment are highlighted. Three different mechanisms for the decomposition of ferrite into sigma phase and secondary austenite are observed during annealing at 800 °C. MFM analysis reveals that a variety of magnetic domain patterns can exist in one ferrite grain.

<https://doi.org/10.1007/s11661-018-4721-1>

© The Minerals, Metals & Materials Society and ASM International 2018

## I. INTRODUCTION

DUPLEX stainless steels represent a very interesting alternative to austenitic-grade stainless steels with almost doubled yield strength, a significantly better resistance to stress-corrosion cracking, and an equal pitting corrosion resistance. In the recent decades, the number of applications for duplex stainless steel has steadily increased in chemical, petrochemical, nuclear, and marine industries.<sup>[1-4]</sup> Duplex stainless steel acquires

its most attractive properties after a controlled solution heat treatment leading to approximately equal volume fractions of  $\delta$  ferrite and  $\gamma$  austenite.<sup>[5]</sup>

Any further heat treatment will change the original phase proportion. In particular, welding procedures can lead to microstructural modifications in the base metal and in the heat-affected zone (HAZ), changing the balance between  $\delta$  and  $\gamma$  phases, and/or causing the precipitation of deleterious phases, such as chromium carbide, chromium nitride, or sigma phase due to steel exposure to temperatures ranging from 300 °C to 1000 °C.<sup>[6-10]</sup>

Among the deleterious phases, sigma phase has a strong embrittlement effect, and only a small quantity of sigma precipitates is enough to significantly reduce the toughness of the alloy. In duplex stainless steels, sigma phase results from the transformation of ferrite into sigma and secondary austenite.<sup>[11]</sup>

Moreover, modifications of the magnetic domain's structure in ferrite with the increasing annealing temperature have been reported in the literature.<sup>[12,13]</sup> However, until now, these effects are still not well understood.

The aim of this study is thus to investigate the influence of heat treatments on the microstructure and magnetic domains in duplex stainless steel S31803. In order to reach this objective, an innovative approach was realized: electron backscatter diffraction (EBSD) maps as well as magnetic force microscopy (MFM) images were acquired on the same region of the sample before and after heat treatment.

---

JEAN DILLE, LUIZ HENRIQUE DE ALMEIDA and JOÃO MARCOS ALCOFORADO REBELLO are with the Metallurgical and Materials Engineering – COPPE - Federal University of Rio de Janeiro Cidade Universitária – Centro de Tecnologia – Bloco F, CEP 21941-914, Rio de Janeiro, Brazil. CLARA JOHANNA PACHECO and CESAR GIRON CAMERINI are with the Laboratory of Nondestructive Testing, Corrosion and Welding, Department of Metallurgical and Materials Engineering, Federal University of Rio de Janeiro, CEP 21941-596, Rio de Janeiro, Brazil. Contact e-mail: cjpacheco@metalmat.ufrj.br LOIC CHARLES MALET is with the 4MAT, Materials Engineering, Characterization, Processing and Recycling, Université Libre de Bruxelles, 50 Avenue FD Roosevelt, CP194/03, Brussels, Belgium. BERNARD NYSTEN is with the Bio and Soft Matter, Institute of Condensed Matter and Nanosciences, Université Catholique de Louvain, Croix du Sud 1/L7.04.02, Louvain-la-Neuve, Belgium. GABRIELA RIBEIRO PEREIRA is with the Metallurgical and Materials Engineering – COPPE - Federal University of Rio de Janeiro Cidade Universitária – Centro de Tecnologia – Bloco F and also with the Laboratory of Nondestructive Testing, Corrosion and Welding, Department of Metallurgical and Materials Engineering, Federal University of Rio de Janeiro.

Manuscript submitted December 22, 2017.

Article published online June 5, 2018

## II. MATERIAL AND METHODS

### A. Chemical Composition

The chemical composition of duplex stainless steel UNS31803 is presented in Table I.

### B. Choice of Heat-Treatment Parameters

The heat-treatment temperatures were selected from the thermodynamic calculation of equilibrium phase fractions as a function of temperature proposed by Bettini *et al.*<sup>[14]</sup> for UNS 32205 duplex stainless steel, having a chemical composition similar to that of UNS 31803 alloy. The corresponding phase stability diagram is shown in Figure 1 and was obtained by means of Thermo-Calc software, using TCFE6 database.

The reference samples have been solubilized at 1120 °C for 1 hour and water quenched in order to contain approximately 50 pct ferrite and 50 pct austenite as indicated on Figure 1. A second annealing heat treatment was then performed on the reference samples. According to the phase stability diagram, annealing for 1 hour at 1260 °C or 1300 °C and water quenching should lead to different volume fractions of  $\alpha$  and  $\gamma$  phases, whereas annealing at 800 °C and water quenching induces also sigma phase precipitation. Different annealing times at 800 °C (from 10 minutes to 2 hours) were applied for a kinetic study of this precipitation.

In order to be able to compare the EBSD and MFM images of the same region, microindentation markers were made on the surface of the sample before applying the heat treatment.

The annealing was then performed in argon atmosphere. This allowed us to avoid polishing the sample after annealing that would have removed the superficial region observed before heat treatment.

### C. Structural Characterization

Optical microscopy (OM) was performed using a Zeiss Axio Imager optical microscope with working station and software for image acquisition, processing, and analysis (Axio Vision and Image Pro). A Zeiss EMA-25 apparatus operating at 30 kV was used for scanning electron microscopy (SEM).

Before OM and SEM analyses, the samples were mechanically polished and electro-etched in a NaOH 20 pct solution at 3 V for 8 seconds.

For each sample, 20 OM images were randomly captured at  $\times 200$  magnification in different regions. Each image corresponds to a  $0.67 \times 0.5$  mm area. The quantitative phase distributions were measured as specified by ASTM E562 standard.<sup>[15]</sup>

EBSD measurements were acquired on a Hitachi SU70 FEG-SEM operated at 20 kV and equipped with an EDAX HIKARI camera. A step size of 150 nm was used. Orientation mapping analyses were done using the TSL OIM software. Samples for EBSD measurement were mechanically polished using diamond paste to reduce them to 1  $\mu\text{m}$  size. Residual stresses were relieved by a final polishing step using a mixture of colloidal silica and water.

Magnetic force microscopy (MFM) characterization was performed at room temperature under ambient conditions using two different equipments. The first one is a Dimension Icon (Bruker<sup>®</sup>) multimode scanning force microscope. MESP magnetic probes (Bruker<sup>®</sup>) with a spring constant between 2.5 and 7.0  $\text{N m}^{-1}$ , a resonance frequency between 65 and 85 kHz, and a quality factor between 200 and 250 were used. Before the analyses, the tips were magnetized using a small magnet. Images with dimensions of  $80 \times 80 \mu\text{m}^2$  and  $30 \times 30 \mu\text{m}^2$  were acquired on the regions marked by indentation in the amplitude-modulation (AM-AFM) lift mode using the following imaging parameters: cantilever-free vibration amplitude,  $A_0 = 40$  nm; set-point amplitude,  $A_{sp} = 35\text{--}38$  nm; lift height  $h_{\text{lift}} = 40\text{--}50$  nm; and a scanning speed of  $30 \mu\text{m s}^{-1}$ . The second MFM equipment is a FlexAFM Nanosurf AG make Cobalt-coated silicon probe (PPP-MFM Nanosensors) with resonant frequency of around 75 kHz was used. The MFM data were acquired in two steps (double pass). Therefore, the MFM tip was magnetized perpendicularly to the sample's surface, prior to the measurements. During the first pass, the topography of the sample was measured in tapping mode. Then, the probe was lifted to a constant distance

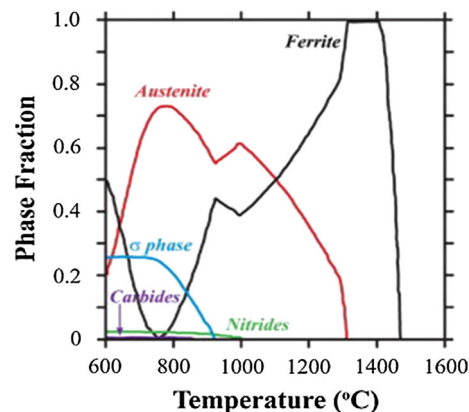


Fig. 1—Phase stability diagram from Bettini *et al.*<sup>[14]</sup> Figure reproduced with permission of Elsevier.

Table I. Chemical Composition of UNS31803 Alloy (in Weight Percent)

Element	C	Si	Mn	Ni	Mo	Cr	Fe
UNS S31803 (Wt Pct)	0.034	0.283	1.78	5.58	2.87	22.02	bal.

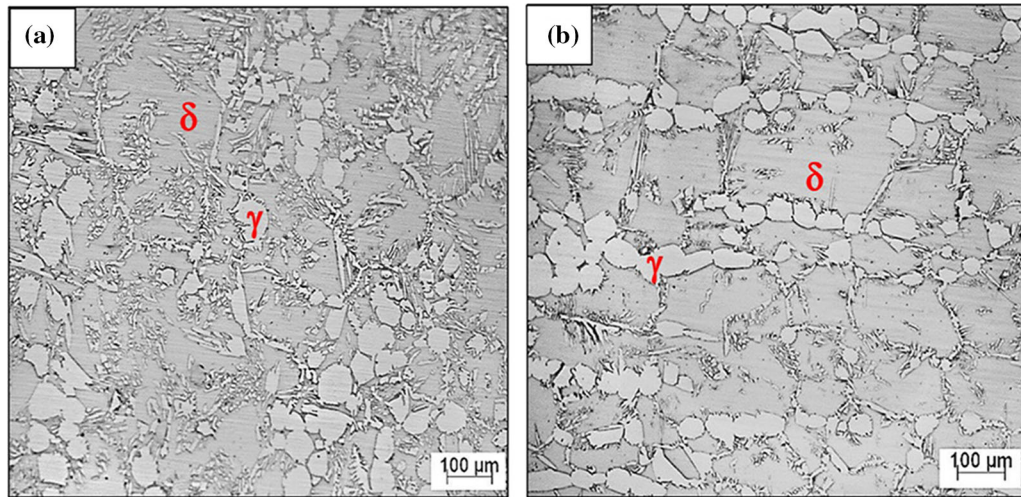


Fig. 2—SEM images of UNS31803 alloy after annealing for 1 h at 1300 °C: (a) air quenched, (b) water quenched.

Table II. Measured and Calculated Phase Volume Fractions

Heat Treatment	Ferrite Measured	Austenite Measured	Sigma Measured	Ferrite ThermoCalc	Austenite ThermoCalc	Sigma ThermoCalc
1300 °C 1 h	79.6	20.4	0.0	85.0	15.0	0.0
1260 °C 1 h	70.1	29.9	0.0	75.0	25.0	0.0
1120 °C 1 h	50.8	49.2	0.0	50.0	50.0	0.0
800 °C 2 h	24.3	52.1	23.6	7.0	73.0	20.0

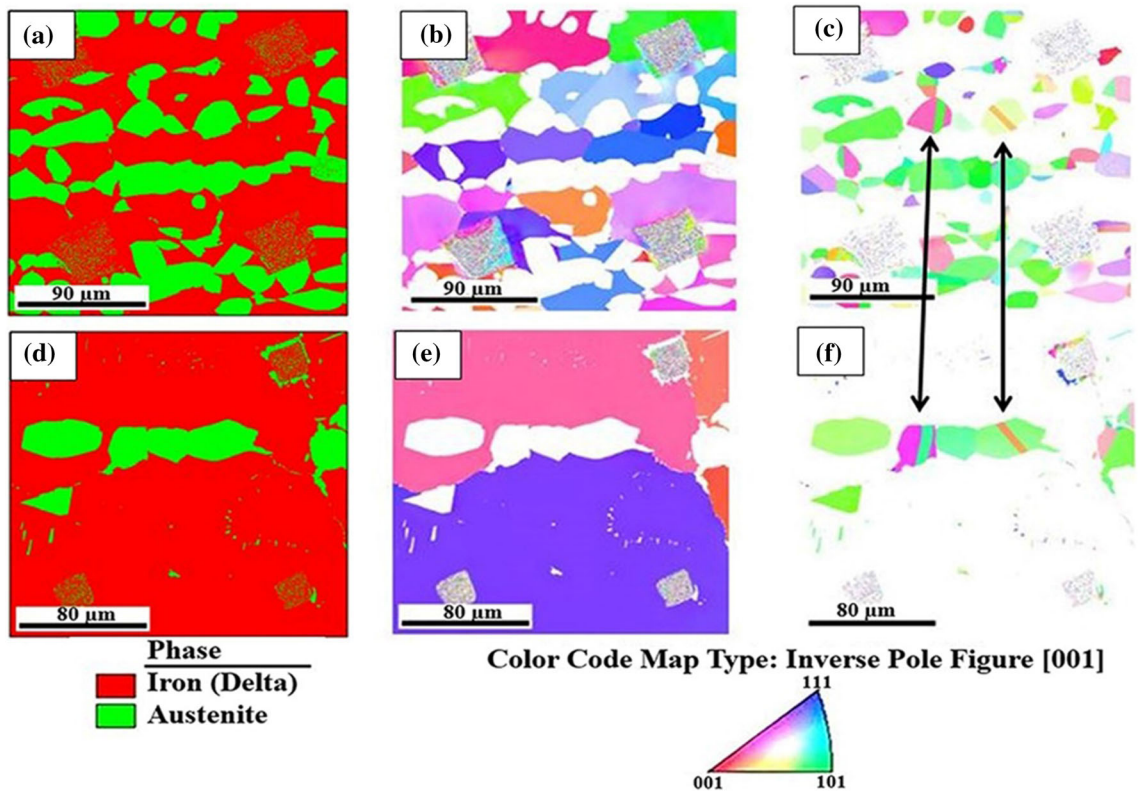


Fig. 3—EBSD analysis of reference sample: (a) phase distribution map, (b) ferrite orientation map, (c) austenite orientation map; EBSD analysis of sample annealed for 1 h at 1260 °C: (d) phase distribution, (e) ferrite orientation map, (f) austenite orientation map.

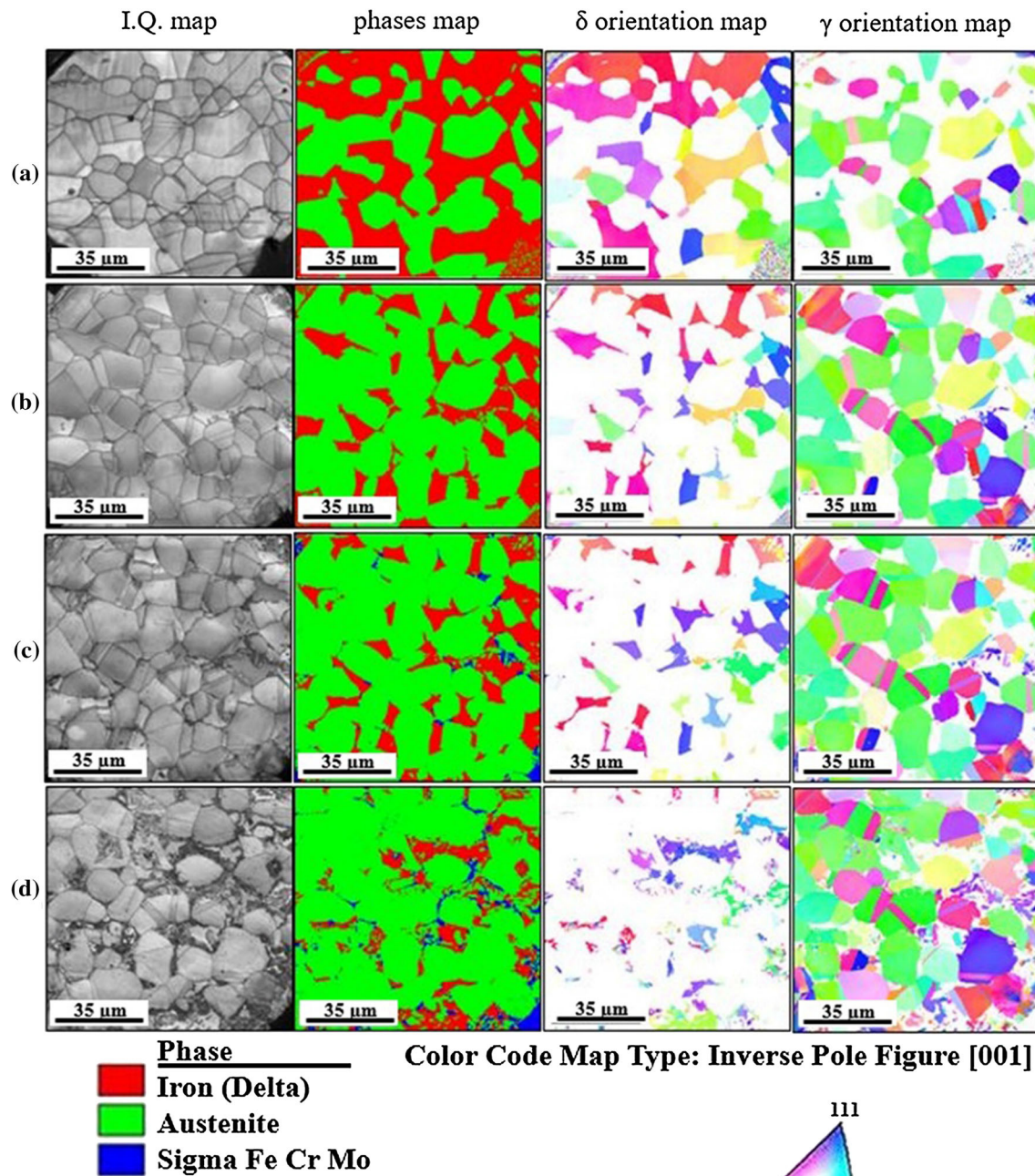


Fig. 4—EBSD analysis of (a) reference sample, (b) sample annealed for 10 min at 800 °C, (c) sample annealed for 30 min at 800 °C, (d) sample annealed for 2 h at 800 °C.

of 110 nm above the sample surface, where magnetic forces are dominant. At this point, the phase-shift induced by the magnetic force gradient between the probe and the sample was recorded, yielding an image of magnetic patterns over the sample surface.

The scans were conducted on an area of 80  $\mu\text{m} \times 80 \mu\text{m}$ . The samples analyzed by MFM were the same previously analyzed by EBSD.

### III. RESULTS AND DISCUSSION

#### A. Influence of Heat Treatment on Phase Volumetric Fractions (Percent)

Table II summarizes the phase volume fractions of each phase after annealing at different temperatures. The measured volume fractions are compared to the volume fractions determined from Thermo-Calc calculations.

The reference sample exhibits the 50 pct ferrite/50 pct austenite microstructure predicted by the phase stability diagram after solubilization for 1 hour at 1120 °C. The austenite volume fractions measured after 1-hour annealing at 1260 °C or 1300 °C are higher than the volume fractions obtained from Thermo-Calc calculations. The difference results from acicular austenite re-precipitation during quenching. Figure 2 indicates that the amount of acicular austenite precipitates depends on the cooling rate after annealing for 1 hour at 1300 °C.

More acicular precipitates are observed after air quenching (Figure 2(a)) than those after water quenching (Figure 2(b)).

After 2-hours annealing at 800 °C, the measured sigma phase volume fraction corresponds to the volume fraction predicted by the phase stability diagram. This confirms the results obtained by Magnabosco.<sup>[16]</sup> The author studied the kinetic of sigma phase formation in UNS31803 duplex stainless steel. On the other hand, the measured ferrite volume fraction is higher than the volume fraction predicted in Figure 1. Ferrite reprecipitation during cooling could occur.

### B. Microstructural Modifications After Heat Treatment

Figure 3 compares the phase distributions and microstructures in the same region before (reference sample) and after annealing at 1260 °C for 1 hour followed by water quenching. The heat treatment modifies the volumetric fractions of ferrite and austenite. Figure 3(a) shows a balanced 50/50 microstructure for the reference sample, whereas the ferrite volumetric fraction increases after annealing at 1260 °C according to Table II (Figure 3(d)). The comparison between the ferrite orientation maps before (Figure 3(b)) and after (Figure 3(e)) the heat treatment reveals that annealing for 1 hour at 1260 °C induces an important ferrite grain growth. Within the observed region, only two ferrite grains subsist at the end of the heat treatment. On the other hand, the austenite orientation maps (Figures 3(c) and (f)) indicate that several austenite grains remain almost unchanged during annealing, whereas others completely disappear. The remaining grains after

annealing for 1 hour at 1260 °C are indicated with arrows on Figure 3.

Figure 4 describes the microstructural evolution during annealing at 800 °C. The Thermo-Calc diagram in Figure 1 predicts sigma phase precipitation at this temperature.

The first column consists of EBSD image quality (IQ) maps. The contrast on these maps provides useful visualization of grain boundaries, permitting the alignment of different images.

The second column shows the phase distribution maps. After annealing for 10 minutes at 800 °C, the austenite volume fraction increases but sigma precipitation is not detected yet. After 30-minutes annealing at 800 °C, sigma precipitates (in blue) are observed, and their volume fraction increases if the heat treatment is prolonged up to 2 hours.

The third and fourth columns are, respectively, the crystallographic orientation maps for ferrite and austenite.

A more careful study reveals several other structural features. Figure 5 shows a region of the sample annealed at 800 °C for 10 minutes. Precipitates are observed in

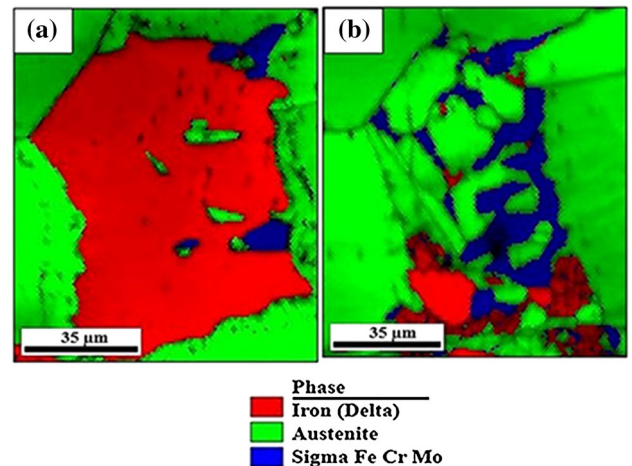


Fig. 6—EBSD phase distribution map of sample annealed at 800 °C for (a) 30 min, (b) 2 h.

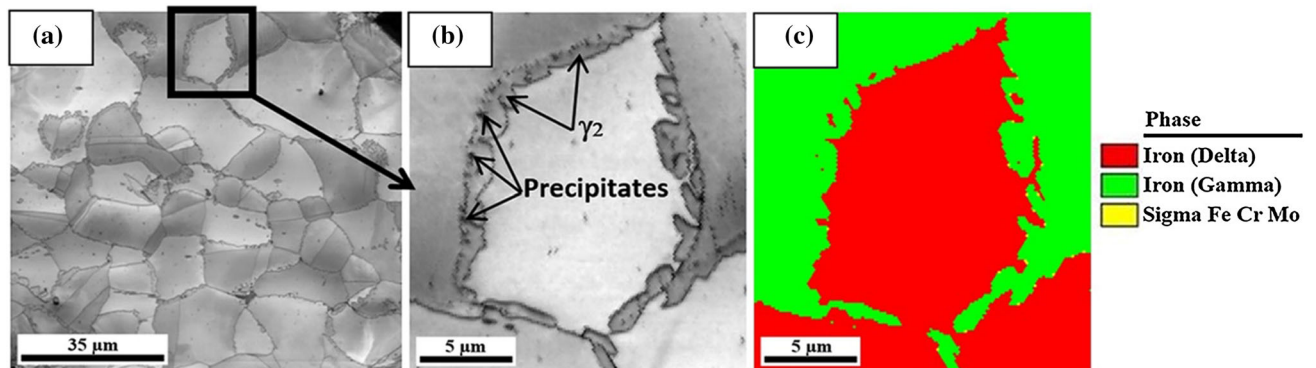


Fig. 5—EBSD analysis of sample annealed for 10 min at 800 °C: (a) IQ map, (b) magnified view of square region showing precipitates and secondary austenite, (c) phase distribution map.

the form of black dots on the EBSD IQ map (Figure 5(a)). According to several authors,<sup>[17,18]</sup> they consist of chromium carbides and nitrides. Most of the precipitates are aligned inside the austenite, close to a ferrite-austenite grain boundary. Chromium carbides and nitrides nucleate preferentially at the initial ferrite-austenite grain boundary in duplex stainless steel. The precipitates grow toward the ferrite. Simultaneously, the adjacent ferrite is transformed into austenite, named “secondary austenite.. The ferrite/austenite interface progressively migrates into the ferrite, leaving the precipitates behind along the original interface. The precipitates and the region corresponding to secondary austenite are indicated by arrows in Figure 5(b).

The corresponding phase distribution map is shown in Figure 5(c). On this map, only ferrite and austenite are identified. It was not possible to index the precipitates by EBSD analysis due to the large interaction volume compared to their size. The precipitation of chromium carbides and nitrides before the formation of sigma phase during isothermal annealing between 700 °C and 900 °C has already been mentioned in different studies.<sup>[19,20]</sup>

On the other hand, the literature indicates that sigma phase forms at ferrite/austenite interfaces and inside ferrite grains.<sup>[21]</sup> The comparison of the same region after 30 minutes at 800 °C and after 2 hours at 800 °C allows us to conclude that sigma phase precipitation at ferrite/austenite interfaces (Figure 6(a)) occurs before sigma phase precipitation inside ferrite grains (Figure 6(b)).

Moreover, the EBSD analyses realized in this study highlight three different mechanisms for the decomposition of ferrite into sigma phase and secondary austenite for stainless steel UNS 31803 at 800 °C.

Figure 7 shows that sigma phase occurs by cellular precipitation, similar to an eutectoid transformation. This first mechanism is already mentioned in the literature.<sup>[22,23]</sup> After 30-minutes annealing at 800 °C, the ferrite decomposition already started at ferrite/austenite interfaces. A couple of sigma and austenite crystals, resulting from ferrite decomposition are indicated on Figure 7(a). The crystallographic orientations for the sigma grain and for the austenite grain are, respectively, represented in Figures 7(b) and (c). Figures 7(e), (f), and (g) reveal the cooperative growth

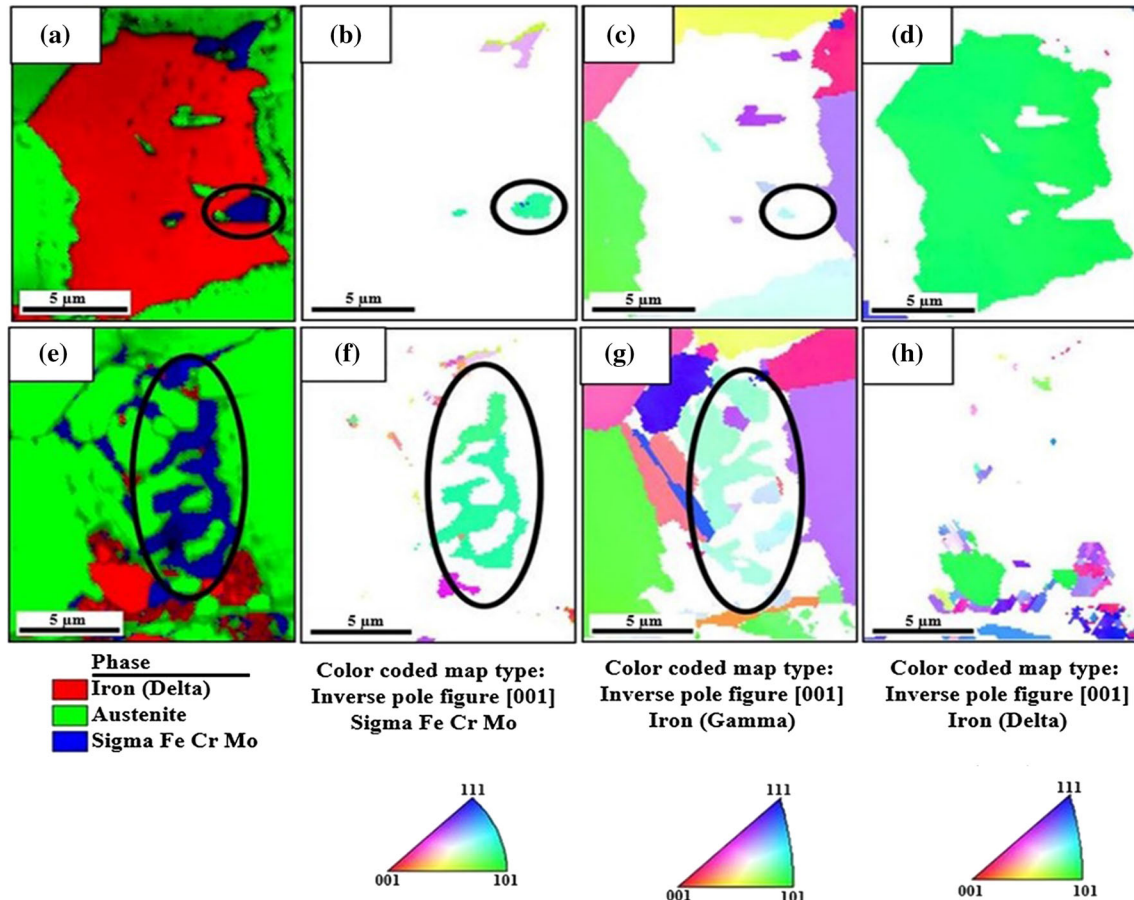


Fig. 7—EBSD analysis of sample annealed at 800 °C for 30 min: (a) phase distribution map, (b) sigma orientation map, (c) austenite orientation map, (d) ferrite orientation map; EBSD analysis of sample annealed at 800 °C for 2 h: (e) phase distribution map, (f) sigma orientation map, (g) austenite orientation map, (h) ferrite orientation map.

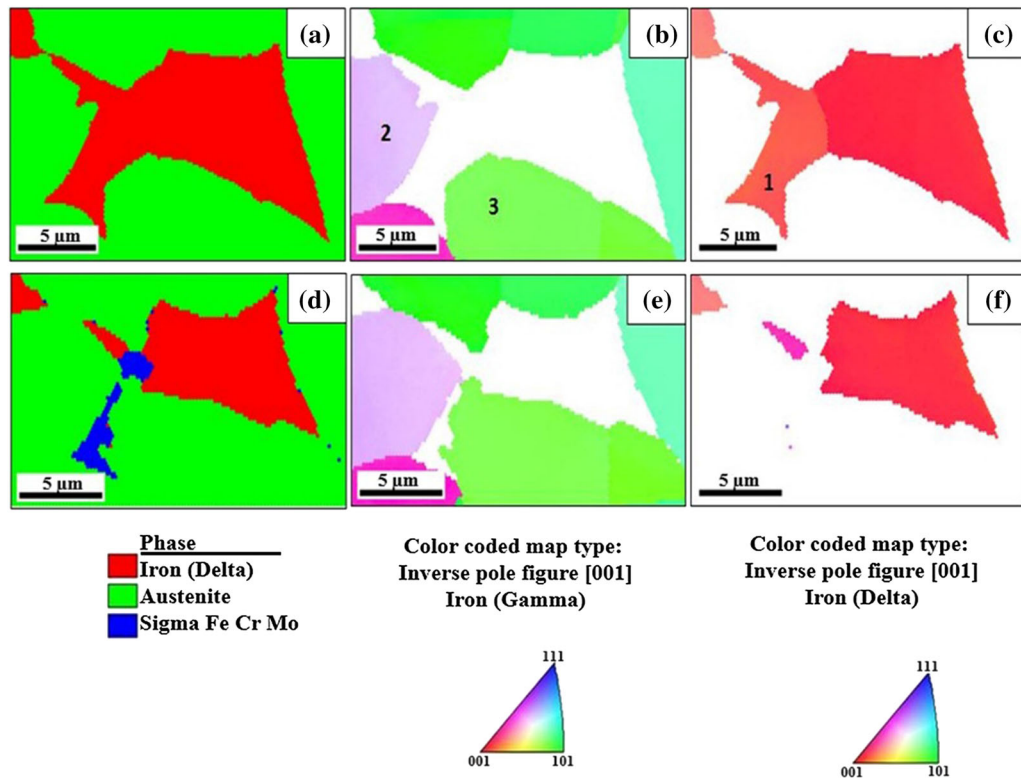


Fig. 8—Second mechanism for sigma precipitation. EBSD analysis of sample annealed at 800 °C for 30 min: (a) phase distribution map, (b) austenite orientation map, (c) ferrite orientation map; EBSD analysis of sample annealed at 800 °C for 2 h: (d) phase distribution map, (e) austenite orientation map, (f) ferrite orientation map.

of the sigma and the austenite crystals inside ferrite after 2 hours at 800 °C.

Figure 8 illustrates a second mechanism for sigma precipitation. During the decomposition of ferrite (grain 1 on Figure 8(c)) into sigma and austenite, the two adjacent austenite grains (2 and 3 on Figure 8(b)) progressively grow. No new austenite grain nucleates. This mechanism of sigma precipitation has not been described in the literature yet.

Figure 9 shows a third mode of decomposition of ferrite during annealing at 800 °C for UNS 31803 stainless steel. Between 30 minutes and 2 hours of annealing at 800 °C, several grains of sigma phase form inside one ferrite grain (grain 1 on Figure 9(c)). They are simultaneously associated with small new austenite grains having different crystallographic orientations (Figure 9(e)). On the other hand, after 30 minutes of annealing at 800 °C, the region analyzed in Figure 9 contains two ferrite grains as shown on the ferrite orientation map (grains 1 and 2 in Figure 9(c)). These two grains decomposed into sigma phase and secondary austenite during ulterior annealing up to 2 hours. After 2 hours, Figure 9(f) reveals that grain 1 is partially decomposed, whereas grain 2 completely disappeared. New ferrite grains are observed on Figure 9(f). It may be assumed that these grains results from ferrite re-precipitation during cooling to room temperature. This explains the difference mentioned in Table II between the measured and the calculated ferrite volume fractions after 2-hours annealing at 800 °C.

### C. Structure of Magnetic Domains in Ferrite

As observed on the MFM image in Figure 10, the magnetic domains inside ferrite grains have a maze-like structure with spikes. This domain structure is typical for ferrite in duplex stainless steels.<sup>[12]</sup>

Figure 11 shows the magnetic domains in ferrite after heat treatment at different temperatures followed by water quenching. No major differences in magnetic domain morphology were observed as a function of annealing temperature. However, after annealing at 1260 °C or 1300 °C, the average thickness of magnetic domains is smaller. In Figure 11, the measured average thickness of magnetic domains in samples annealed at 800 °C, 1120 °C, 1260 °C, and 1300 °C, are, respectively,  $0.91 \pm 0.17 \mu\text{m}$ ,  $1.56 \pm 0.25 \mu\text{m}$ ,  $0.72 \pm 0.37 \mu\text{m}$ , and  $0.64 \pm 0.21 \mu\text{m}$ . This result has already been mentioned by Lo.<sup>[12]</sup> The author proposed two possible explanations: the higher residual stresses associated with quenching from a higher temperature; the small changes in partition coefficients of alloying elements between ferrite and austenite as a function of temperature.

In the current study, the magnetic domain structures in water quenched and air quenched samples after annealing for 1 hour at 1300 °C are compared. No difference in magnetic domain width was detected as shown in Figure 12. For this reason, it can be concluded that the residual stresses associated with quenching from high temperature do not have any influence on the magnetic

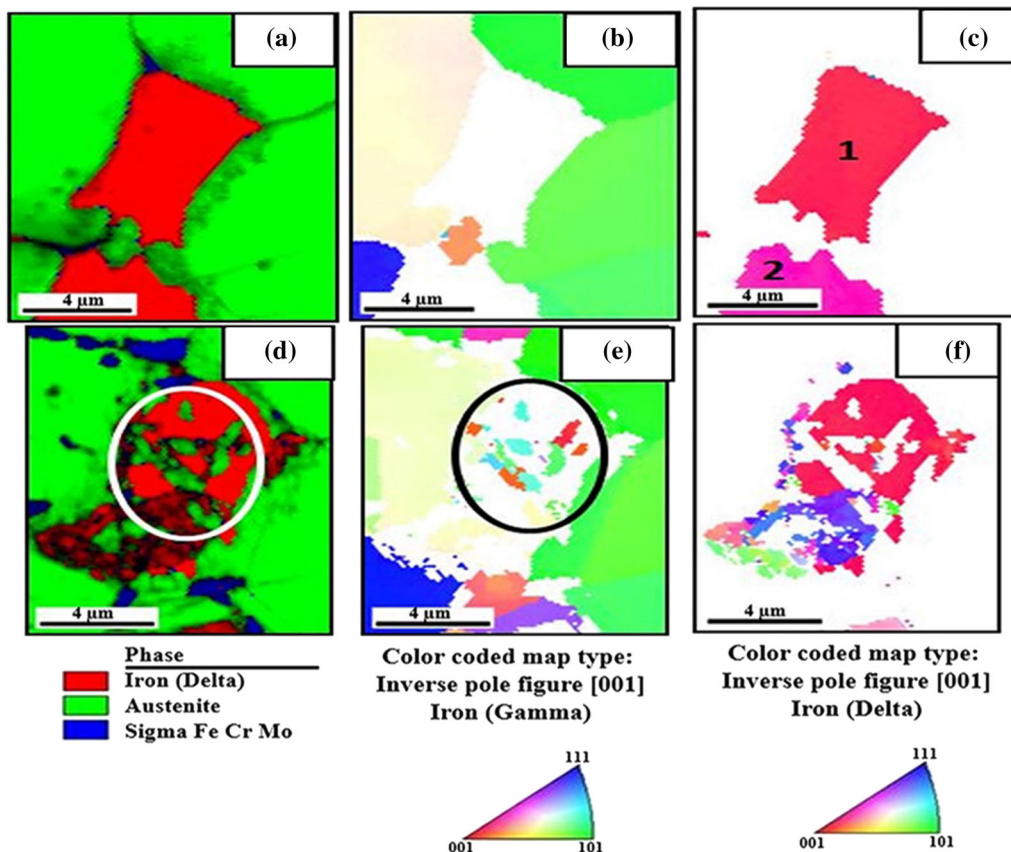


Fig. 9—Third mode of decomposition of ferrite during annealing. EBSD analysis of sample annealed at 800 °C for 30 min: (a) phase distribution map, (b) austenite orientation map, (c) ferrite orientation map; EBSD analysis of sample annealed at 800 °C for 2 h: (d) phase distribution map, (e) austenite orientation map, (f) ferrite orientation map.

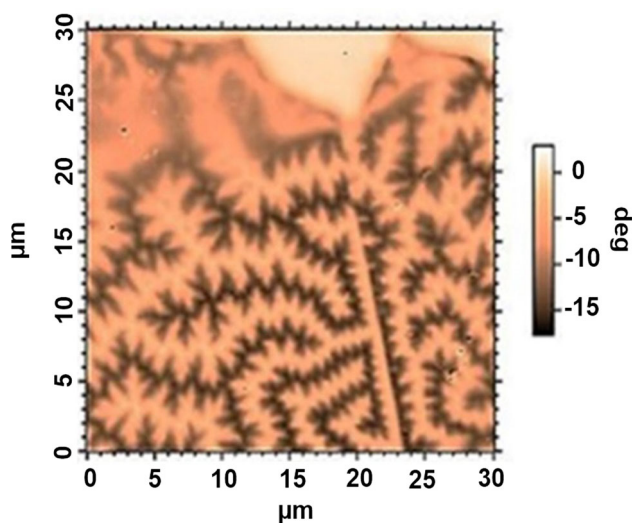


Fig. 10—MFM images of magnetic domains in ferrite showing maze-like pattern with spikes.

domain width. Only the hypothesis of the influence of small changes in chemical composition could remain.

Figure 13 compares EBSD map and MFM image of a same region. The magnetic domain pattern in ferrite is associated with crystal anisotropy and, therefore, related to

the crystallographic orientation.<sup>[13]</sup> In Figure 13, ferrite grains with different crystallographic orientations exhibit different magnetic domain patterns. Moreover, different magnetic domain patterns corresponding to one unique crystallographic orientation are observed. The ferrite grain inside the dashed rectangle is represented on the ferrite orientation map in Figure 13(b) by a unique color (blue). This means that this entire ferritic region has the same [111] crystallographic orientation perpendicular to the surface of the sample. In order to assert that ferrite inside the dashed rectangle is truly a monocrystal, it is necessary to verify that there is no misorientation by rotation around this axis. Figure 14 shows the misorientation profile from point 1 to point 2 along the white line in Figure 13(b). This misorientation profile was obtained from EBSD measurements and reveals that there is no point-to-point misorientation exceeding 0.6 deg. In conclusion, the ferrite inside the dashed rectangle can be considered as a monocrystal but presents different magnetic domain patterns as seen on the MFM image in Figure 13b.

#### IV. CONCLUSIONS

After solubilization for 1 hour at 1120 °C followed by water quenching, the UNS31803 duplex stainless steel exhibits the 50 pct ferrite/50 pct austenite microstructure predicted by its phase stability diagram.



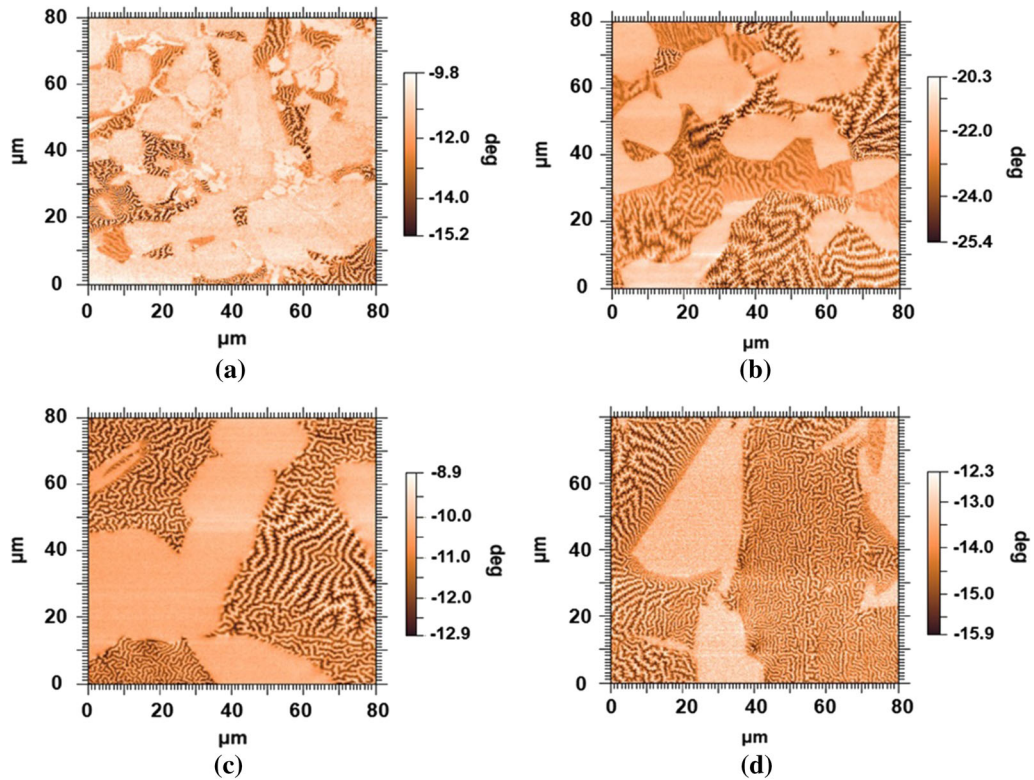


Fig. 11—MFM images of sample annealed at (a) 800 °C, (b) 1120 °C, (c) 1260 °C, (d) 1300 °C.

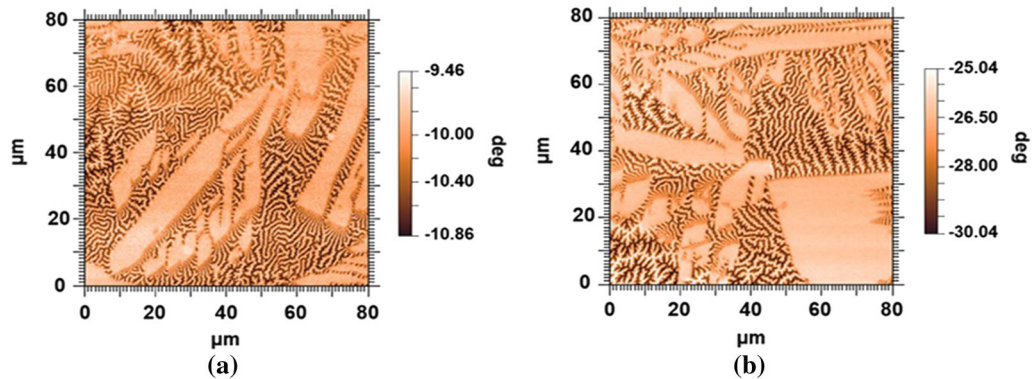


Fig. 12—MFM images of samples annealed for 1 h at 1300 °C: (a) water-quenched, (b) air-quenched.

The innovative comparison of EBSD maps and MFM images of the same region before and after ulterior heat treatment permits to obtain the main results as follows:

1. During annealing at 1260 °C, an important ferrite grain growth is observed, whereas several austenite grains remain almost unchanged and others completely disappear.
2. During annealing at 800 °C, sigma phase precipitation at ferrite/austenite interfaces occurs before sigma precipitation inside ferrite grains.
3. Three different mechanisms for the decomposition of ferrite into sigma phase and secondary austenite are observed for stainless steel UNS 31803 at 800 °C: (1) eutectoid decomposition, (2) sigma precipitation with growth of adjacent pre-existing austenite grains, (3) formation of several sigma grains inside one ferrite grain associated with formation of small new austenite grains.
4. Ferrite grains with different crystallographic orientations exhibit different magnetic domain patterns.
5. It has been observed that one ferrite grain can contain different magnetic domain patterns.

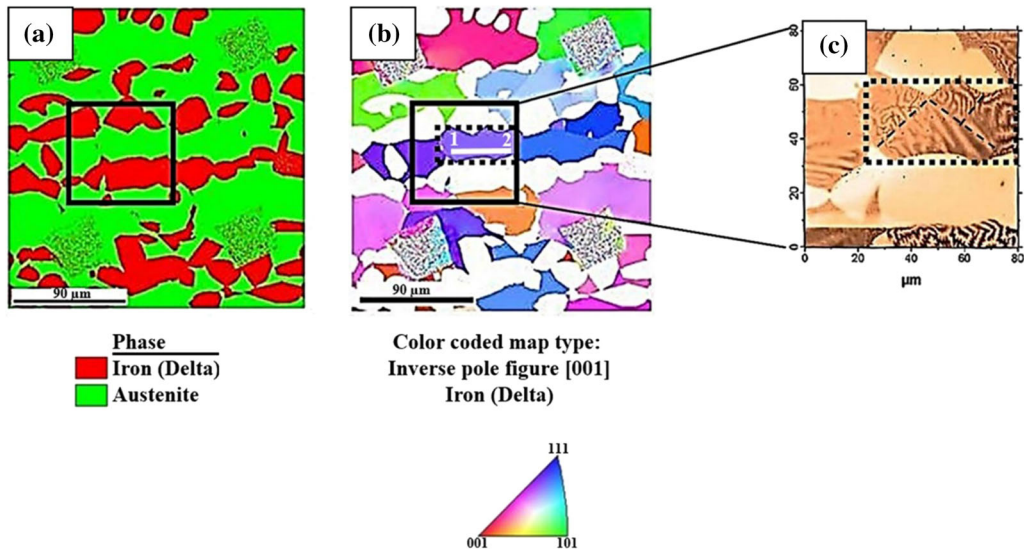


Fig. 13—(a) EBSD phase distribution map of reference sample, (b) ferrite orientation map, (c) MFM image of square region.

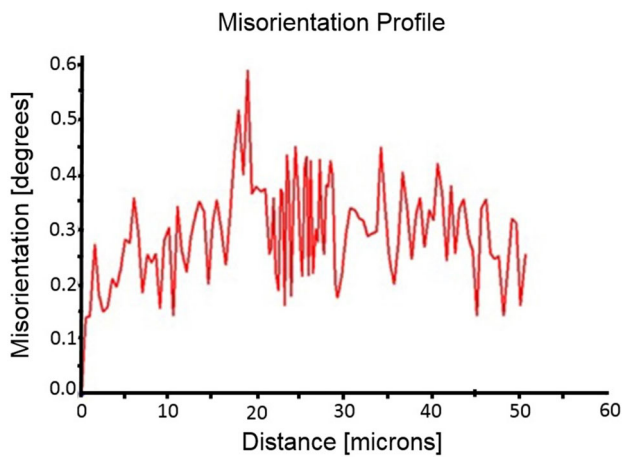


Fig. 14—Misorientation profile from point 1 to point 2 on Fig. 13(b).

## ACKNOWLEDGMENTS

The authors offer their thanks to the Brazilian research agencies (CAPES, FAPERJ, FINEP, and CNPq) and Wallonie-Bruxelles International (WBI) for their financial support.

## REFERENCES

1. ASM Speciality Handbook: *Stainless Steels*, American Society for Metals, Metals Park, OH, 1994.
2. J. Charles: *Duplex Stainless Steel '97 International Conference & Expo*, Maastricht, the Netherlands, 1997, pp. 29–42.

3. R.N. Gunn: *Duplex Stainless Steel: Microstructure, Properties and Applications*, Abington Publishing Cambridge, Abington, 1997, p. 204.
4. API Technical Report 938-C, API-American Petroleum Institute, Use of duplex stainless steels in the oil refining industry, 2005.
5. J.M.A. Rebello, M.C.L. Areiza, C.G. Camerini, and J.V. Rocha: *Proceedings of the IEEE*, 2013, vol. 1, pp. 13845445-7.
6. I Calliari, E Ramous, and P Bassani: *Mater. Sci. Forum*, 2010, vols. 638–642, pp. 2986–91.
7. SSM Tavares, MR da Silva, and JM Neto: *J. Alloys Compd*, 2000, vol. 313, pp. 168–73.
8. C-C Hsieh and W Wu: *ISRN Metall.*, 2012, vol. 2012, p. 16.
9. J-Y Maetz, S Cazottes, C Verdu, and X Kleber: *Metall. Mater. Trans. A*, 2016, vol. 47A, pp. 239–53.
10. KH Lo, CH Shek, and JKL Lai: *Mater. Sci. Eng. R*, 2009, vol. 65, pp. 39–104.
11. H Sieurin and R Sandström: *Mater. Sci. Eng. A*, 2007, vol. 444, pp. 271–76.
12. KH Lo: *Mater. Charact.*, 2012, vol. 72, pp. 66–72.
13. LQ Guo, XM Zhao, M Li, WJ Zhang, Y Bai, and LJ Qiao: *Appl. Surf. Sci.*, 2012, vol. 259, pp. 213–18.
14. E Bettini, U Kivisäkk, C Leygraf, and P Jinshan: *Electrochim. Acta*, 2013, vol. 113, pp. 280–89.
15. ASTM E562 “Standard Test Method for Determining Volume Fraction by Systematic Manual Point Count, 2001.
16. R Magnabosco: *Mater. Res.*, 2009, vol. 12, pp. 321–27.
17. J.-Y. Maetz, T. Douillard, S. Cazottes, C. Verdu, and X. Kleber, *Micron*, 2016, pp. 43–53.
18. AJ Ramirez, JC Lippold, and SD Brandi: *Metall. Mater. Trans. A*, 2003, vol. 34A, pp. 1575–97.
19. R Badji, M Bouabdallah, B Bacroix, C Kahloun, K Bettahar, and N Kherrouba: *Mater. Sci. Eng. A*, 2008, vol. 496, pp. 447–54.
20. I Zucato, MC Moreira, IF Machado, and S Giampietri: *Lebrão-Mater. Res.*, 2002, vol. 5, pp. 385–89.
21. AF Padilha, DJM Aguiar, and RL Plaut: *Defect Diffus. Forum*, 2012, vols. 163–174, pp. 163–74.
22. P Ferro and F Bonollo: *Metall. Mater. Trans. A*, 2012, vol. 43A, pp. 1109–16.
23. JW Elmer, TA Palmer, and ED Specht: *Metall. Mater. Trans. A*, 2007, vol. 38A, pp. 464–75.